Explicitly determined sea ice emissivity and emission temperature over the Arctic for surface-sensitive microwave channels

Kang, Eui-Jong; Sohn, Byung-Ju; Tonboe, Rasmus Tage; Noh, Young-Chan; Kwon, In-Hyuk; Kim, Sang-Woo; Maturilli, Marion; Kim, Hyun-Cheol; Liu, Chao

Published in:
Quarterly Journal of the Royal Meteorological Society

Link to article, DOI:
10.1002/qj.4492

Publication date:
2023

Document Version
Publisher's PDF, also known as Version of record

Received: 27 June 2022 | Revised: 11 April 2023 | Accepted: 12 April 2023 | Published on: 7 June 2023

DOI: 10.1002/qj.4492

Quarterly Journal of the Royal Meteorological Society RMetS

RESEARCH ARTICLE

Explicitly determined sea ice emissivity and emission temperature over the Arctic for surface-sensitive microwave channels

Eui-Jong Kang[1] | **Byung-Ju Sohn**[1,2] | **Rasmus Tage Tonboe**[3] | **Young-Chan Noh**[4] | **In-Hyuk Kwon**[5] | **Sang-Woo Kim**[1] | **Marion Maturilli**[6] | **Hyun-Cheol Kim**[4] | **Chao Liu**[2]

[1]School of Earth and Environmental Sciences, Seoul National University, Seoul, South Korea

[2]School of Atmospheric Physics, Nanjing University of Information Science and Technology (NUIST), Nanjing, China

[3]National Space Institute, Danish Technical University, Copenhagen, Denmark

[4]Korea Polar Research Institute, Incheon, South Korea

[5]Korea Institute of Atmospheric Prediction Systems, Seoul, South Korea

[6]Helmholtz Centre for Polar and Marine Research, Alfred Wegener Institute, Bremerhaven, Germany

Correspondence
Byung-Ju Sohn, School of Atmospheric Physics, Nanjing University of Information Science and Technology (NUIST), Nangliu Road, Nanjing, Jiangsu, China
Email: sohn@snu.ac.kr

Funding information
National Research Foundation of Korea (NRF) grant funded by the Korea government (MSIT), Grant/Award Number: NRF-2021R1A4A5032320; R&D project on the Development of a Next-generation Data Assimilation System of the Korea Institute of Atmospheric Prediction Systems (KIAPS) funded by the Korea Meteorological Administration (KMA), Grant/Award Number: KMA2020-02211

Abstract

Data assimilation of satellite microwave measurements is one of the important keys to improving weather forecasting over the Arctic region. However, the use of surface-sensitive microwave-sounding channel measurements for data assimilation or retrieval has been limited, especially during winter, due to the poorly constrained sea ice emissivity. In this study, aiming at more use of those channel measurements in the data assimilation, we propose an explicit method for specifying the surface radiative boundary conditions (namely emissivity and emitting layer temperature of snow and ice). These were explicitly determined with a radiative transfer model for snow and ice and with snow/ice physical parameters (i.e. snow/ice depths and vertical distributions of temperature, density, salinity, and grain size) simulated from the thermodynamically driven snow/ice growth model. We conducted 1D-Var experiments in order to examine whether this approach can help to use the surface-sensitive microwave temperature channel measurements over the Arctic sea ice region for data assimilation. Results show that (1) the surface-sensitive microwave channels can be used in the 1D-Var retrieval, and (2) the specification of the radiative boundary condition at the surface using the snow/sea ice emission model can significantly improve the atmospheric temperature retrieval, especially in the lower troposphere (500 hPa to surface). The successful retrieval suggests that useful information can be extracted from surface-sensitive microwave-sounding channel radiances over sea ice surfaces through the explicit determination of snow/ice emissivity and emitting layer temperature.

KEYWORDS

1D-Var retrieval, Arctic winter sea ice, data assimilation, emissivity, emitting layer temperature, microwave temperature sounding, snow and sea ice model

1 | INTRODUCTION

Data assimilation for numerical weather prediction (NWP) has been one of the major scientific achievements in improving weather forecasts over the past decades (Bauer *et al.*, 2015). However, the weather prediction over the sea ice-covered Arctic Ocean is not equally successful because the initial state is less accurate due to the lack of *in situ* observations compared with other regions covered with land or open water (Bauer *et al.*, 2016; Jung and Matsueda, 2016; Bormann *et al.*, 2017). With growing interest in the weather prediction in polar regions in conjunction with rapid global warming (Jung *et al.*, 2016) and possible influences of polar changes on the weather/climate in lower latitudes (Jung *et al.*, 2014; Semmler *et al.*, 2018; Day *et al.*, 2019; Laroche and Poan, 2022), the poor data assimilation performance over the Arctic has received considerable attention in recent years (WMO, 2013; Sandu *et al.*, 2021).

Due to the lack of *in situ* observations, the data assimilation over the Arctic Ocean heavily relies on satellite measurements. In fact, the Arctic region has advantages of more temporal coverage in polar-orbiting satellite measurements than over lower latitudes. Among the various satellite measurements used for data assimilation in NWP, microwave radiometer measurements are more readily used because of the less sensitive nature of microwave to clouds, compared to cloud-sensitive infrared measurements (Jiménez *et al.*, 2017; Lawrence *et al.*, 2019). The impact of microwave observations on forecasts in the Arctic region is found to be greatest amongst all available observations during the summer, but during the winter, the conventional observations give the largest impact, followed by microwave observations (Lawrence *et al.*, 2019). The reduced impact of microwave measurements during the winter is due to the difficulties in characterizing the radiative properties of snow and ice. Consequently, the use of microwave measurements during the winter has been largely limited to channels that are not affected by the surface, wasting surface-sensitive channel measurements, which are important for providing thermal information of the mid- to lower troposphere.

The difficulties of assimilating surface-sensitive microwave measurements over the Arctic sea ice region during the winter largely stem from the fact that microwave emission is from within the snow/ice layer. The upwelling microwave radiation at the snow surface is from emission and scattering by the same snow/ice layer that the microwaves penetrate. Because of that, for the data assimilation, the emissivity and emitting layer temperature of the snow/ice layer should be known for providing the proper surface boundary condition to the radiative transfer model to calculate the brightness temperature (TB) at the top of the atmosphere (TOA).

In the atmosphere–snow/ice–ocean coupled model, it should be ideal to produce detailed snow/ice microphysics from which the snow/ice emission and scattering can be directly calculated and incorporated into the radiative transfer forward model. In this direction, satellite-measured microwave radiances can be assimilated in a sense that the snow and ice are an integral part of the coupled atmosphere–snow/ice–ocean system. Aiming at more use of surface-sensitive microwave channels for the data assimilation, we explore this approach to obtain physically consistent emissivity of snow and ice and associated emitting layer temperature, by explicitly and seamlessly calculating the radiative transfer in the atmosphere and within the snow/ice layers. This may be called an "explicit method" and it is thought to be physically consistent with microwave radiometer measurements.

This explicit method requires the optical properties of snow and ice for calculating the radiative transfer within the snow/ice layers. However, because the current NWP models are not capable of producing optical properties of snow and ice, we obtain that information from simulations using a thermodynamic snow/ice growth model constrained by satellite-derived surface temperature and snow/ice interface temperature (Kang *et al.*, 2021). Thus, although this model is loosely linked to the NWP model through the imposed surface fluxes and precipitation provided by the NWP model, the functioning of the model is independent of the NWP model.

In this study, we estimate multi-spectral emissivities and associated emission temperatures for Advanced Technology Microwave Sounder (ATMS) temperature-sounding channels, with information and constraints from the thermodynamic growth model and radiative transfer model for the snow and ice. With this obtained information, once atmospheric profiles are given, TOA TBs for surface-sensitive microwave-sounding channels are calculated. Here, for the radiative transfer calculation, only the clear-sky condition is assumed. We first investigate how this approach can give impact on temperature retrievals with a one-dimensional variation (1D-Var) standalone system over the Arctic sea ice region. We hypothesize that temperature retrieval should be improved if the physically consistent snow/ice emissivity and emitting layer temperature can provide a better lower boundary condition for the radiative transfer calculation. Proving the hypothesis, temperature profiles are retrieved from surface-insensitive microwave temperature-sounding channels only, as well as from temperature-sounding channels including the surface-sensitive channels, using the 1D-Var scheme.

Aiming at advances in the polar prediction capacity, this article has centred on data assimilation amongst the comprehensive priorities for Arctic forecasting: observation, modelling, data assimilation, ensemble forecasting, predictability and forecast error diagnosis, global linkage, and verification (WMO, 2013). The main objective is to explore if this explicit approach to combining the thermodynamic snow/ice growth model with the radiative transfer model enables us to provide a well-defined surface boundary and then ultimately to open up possibilities of the coupled data assimilation. The remainder is organized as follows. Section 2 introduces the data used, and Section 3 describes the explicit method for estimating emissivity and emitting layer temperature of snow and ice. Then, the design of 1D-Var experiments and retrieval results follow in Sections 4 and 5, and conclusions are given in Section 6.

2 | DATA USED

All necessary data for this study are collocated with radiosonde observations taken along the drift trajectory of the Multidisciplinary drifting Observatory for the Study of Arctic Climate (MOSAiC) expedition from December 2019 to March 2020 (Maturilli *et al.*, 2021). The trajectory of the MOSAiC expedition is given in Figure 1. Datasets used in this study and construction of collocated datasets are as follows.

2.1 | Model-produced snow/ice parameters

In Kang *et al.* (2021), the 1D thermodynamic diffusion model was implemented and extended into the 2D spatial and temporal domains by employing Lagrangian tracking of drifting Arctic ice targets. The one-dimensional column model computes the snow/ice profile at a specific time and location, and by employing the 1D model while following the drifting ice it was possible to depict a four-dimensional view of snow/ice profile development. The model was forced by ERA5 atmospheric reanalysis data on surface level (Hersbach *et al.*, 2020) and was constrained by nudging satellite-derived surface temperature (Dybkjær *et al.*, 2018) and snow/ice interface temperature (Lee and Sohn, 2015). The tracking of ice drift was based on the satellite-derived ice drifting vector (Lavergne *et al.*, 2010). The snow/ice growth model consists of independent snow and ice systems which have respective multiple layers with a 1–3 cm vertical resolution. The snowfall, provided as an atmospheric input, is considered a newly accumulated snow layer over the pre-existing snow layers. The heat transfer within the snow and ice responds to the heat fluxes provided at snow-top and ice-bottom boundaries, leading to ice growth. Simulations of physical parameters using the scheme developed by Kang *et al.* (2021) provide 3 hr snow/ice depths and profiles of temperature, density, salinity, and grain size. The model simulation results during winter demonstrated that the Kang *et al.* approach could successfully simulate the evolution of the physical parameters of snow and ice over the Arctic Ocean during the winter. Detailed descriptions regarding the snow/ice growth model, required inputs, and model performance are found in Kang *et al.* (2021) and references therein.

In this study, the surface boundary condition needed for running the atmospheric radiative transfer will be obtained from physical parameters simulated with the Kang *et al.* approach, along the MOSAiC drifting track (Figure 1). The model simulation started for the ice target (whose size is 25×25 km) collocated with the position of MOSAiC observation site on 1 October 2019. Then, the simulation was continued until 31 March along the drift of the selected ice target, which was determined by satellite-derived ice motion vectors using the Lagrangian tracking method. It is shown that the estimated trajectory of the ice target (blue line in Figure 1a) is in good agreement with the trajectory of the MOSAiC site (red line in Figure 1a), and the differences between two trajectories at a given time are found to be within 30 km (Figure 1b). As in Kang *et al.* (2021), the first 2 months of the simulations (i.e. October and November) are considered as a spin-up period to allow the model's snow/ice system to fully respond to the given inputs. Thus, along the MOSAiC track, the snow/ice physical parameters are produced over a 4-month period (i.e. December–March).

2.2 | AMSR2 brightness temperatures

We combine an optimization procedure with the snow/ice emission model (i.e. radiative transfer model for the snow and ice) in order to optimally determine the optical properties of snow and ice. The optimization is achieved by altering optical properties and comparing the simulated TOA TBs against Advanced Microwave Scanning Radiometer 2 (AMSR2)-measured TBs; the detailed optimization procedures are given in Section 3. The AMSR2, flown on the Global Change Observation Mission for Water (GCOM-W) satellite launched in 2012, is a multi-purpose microwave radiometer comprising 14 channels at 7 window frequencies with 55° conically scanning type (JAXA, 2015; see Table 1 for the AMSR2 specifications). Amongst 14 channels of Level 1R AMSR2 TBs whose centre position of all channel footprints is modified to coincide at the centre of 89 GHz (Maeda *et al.*, 2015),

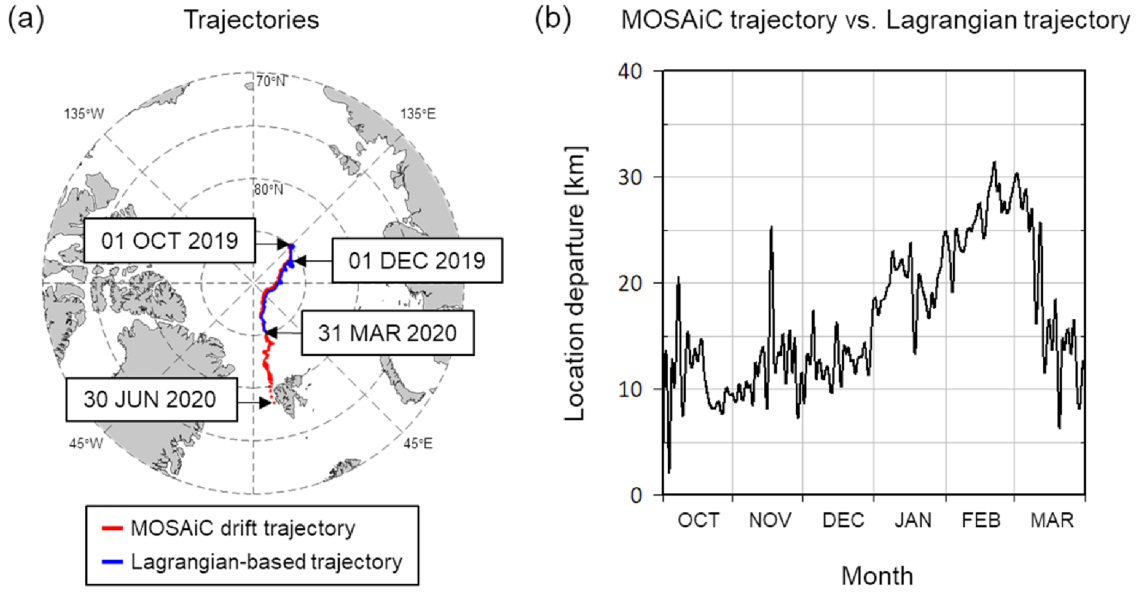

FIGURE 1 (a) Geographical comparison of multidisciplinary drifting observatory for the study of Arctic climate (MOSAiC) expedition trajectory (red) with the corresponding Lagrangian-based trajectory estimation (blue) during the analysis period from October 2019 to March 2020. (b) Difference between two trajectories on a daily time-scale. The MOSAiC trajectory is the 1 October 2019 to 30 June 2020 portion [Colour figure can be viewed at wileyonlinelibrary.com]

TABLE 1 Specific characteristics of the advanced microwave scanning radiometer-2 (AMSR2) instrument

No.	Central frequency (GHz)	Bandwidth (MHz)	Polarization	Resolution (km^2)
1	6.925	350	H	35 × 62
2	6.925	350	V	35 × 62
3	7.3	350	H	35 × 62
4	7.3	350	V	35 × 62
5	10.65	100	H	24 × 42
6	10.65	100	V	24 × 42
7	18.7	200	H	14 × 22
8	18.7	200	V	14 × 22
9	23.8	400	H	11 × 19
10	23.8	400	V	11 × 19
11	36.5	1000	H	7 × 12
12	36.5	1000	V	7 × 12
13	89.0	3000	H	3 × 5
14	89.0	3000	V	3 × 5

we use 10 channels, that is, 10.7, 18.7, 23.8, 36.5 and 89.0 GHz Vertical(V)/Horizontal(H)-polarization(pol) with a frequency-dependent spatial resolution of 5–62 km.

2.3 | MOSAiC radiosonde data

During the MOSAiC expedition, vertical profiles of pressure, temperature and relative humidity were obtained by radiosondes, four times per day (Maturilli *et al.*, 2021). A total of 470 radiosonde launches were made during the analysis period between 1 December 2019 and 31 March 2020. Among the 470 radiosonde observations, 464 observations are kept, covering at least up to the 100 hPa level. These are then defining the true state for the 1D-Var experiment.

2.4 | ERA5 reanalysis data

Since the radiosonde measurements normally extend high up to the 100 hPa level or a little higher, atmospheric states

above radiosonde measurements are needed for constructing the true state including the stratospheric level. Data above the radiosonde's highest level are obtained from the ERA5 hourly-based reanalysis data of the European Centre for Medium-Range Weather Forecasts (ECMWF) (Hersbach *et al.*, 2020). The temperature and humidity profiles used are given in 37 pressure levels and $0.25° \times 0.25°$ latitude–longitude grid on an hourly time-scale.

2.5 | ATMS brightness temperatures

The ATMS window channel TBs are used as a reference dataset for examining the simulated TBs based on the explicit method, while ATMS temperature-sounding channel TBs are used as an observation state in the 1D-Var experiment for demonstrating a prerequisite for other applications. The ATMS, flown on the National Oceanic and Atmospheric Administration-20 (NOAA-20) satellite launched in 2017, is a temperature and humidity sounder consisting of 19 channels at 54 GHz oxygen and 183 GHz water vapour absorption bands and 3 window channels at 23, 31 and 89 GHz (Weng *et al.*, 2012) – see Table 2 for the ATMS specifications. Due to the cross-track scanning, each scan position is divided into 96 steps within 2,200 km of the swath, with the zenith angle ranging from −65° to 65°. We use Level 1B ATMS TBs in the spatial resolution of 16–75 km.

2.6 | TELSEM2 monthly sea ice emissivity

The impact of explicitly calculated snow/ice emissivity and emitting layer temperature on the TB simulation is examined by comparing TB simulation with those from the use of Tool to Estimate Land Surface Emissivity from Microwave to submillimetre waves (TELSEM2: Wang *et al.*, 2017). TELSEM2 provides a monthly climatology of the sea ice emissivities over 5–700 GHz frequency range. The climatology is based on satellite-derived emissivities from the Special Sensor Microwave Imager (SSM/I), Advanced Microwave Sounding Unit-B (AMSU-B), and Special Sensor Microwave Imager/Sounder (SSMIS) monthly observations for 19–190 GHz. The TELSEM2 was evaluated by aircraft measurements, but it was reported that the validation results are inconclusive for the sea ice areas (Wang *et al.*, 2017). Surface emissivities along the MOSAiC trajectory are obtained by running the TELSEM2.

2.7 | Construction of collocated datasets

Since the experiments are conducted along the MOSAiC trajectory, in conjunction with the MOSAiC radiosonde observations, all data used are collocated with radiosonde observations. In this collocation, radiosonde observations are considered vertical and instantaneous at the launch location and time. Considering that four-times-daily

TABLE 2 Specific characteristics of the advanced technology microwave sounder (ATMS) instrument. Only channels below 60 GHz are provided

No.	Central frequency (GHz)	Bandwidth (MHz)	Quasi-polarization	Resolution (km^2)
1	23.8	270	QV	75×75
2	31.4	180	QV	75×75
3	50.3	180	QH	32×32
4	51.76	400	QH	32×32
5	52.8	400	QH	32×32
6	53.596 ± 0.115	170	QH	32×32
7	54.4	400	QH	32×32
8	54.94	400	QH	32×32
9	55.5	330	QH	32×32
10	$f0 = 57.290344$	330	QH	32×32
11	$f0 \pm 0.217$	78	QH	32×32
12	$f0 \pm 0.3222 \pm 0.048$	36	QH	32×32
13	$f0 \pm 0.3222 \pm 0.022$	16	QH	32×32
14	$f0 \pm 0.3222 \pm 0.010$	8	QH	32×32
15	$f0 \pm 0.3222 \pm 0.0045$	3	QH	32×32

radiosonde measurements generally represent synoptic atmospheric conditions, the spatial difference of 30 km and the temporal difference of 90 min are considered to be criteria for constructing the collocated datasets.

Because the departures of the ice target for the diffusion model simulation are within at most 30 km (Figure 1b), the model-simulated physical parameters can be counted on as collocated with the MOSAiC radiosonde observations within the 90 min time difference. Hourly ERA5 reanalysis data are in 0.25°×0.25° grid format, and thus, collocated data are found by selecting the grid value in the closest location from the MOSAiC radiosonde observations within the 30 min time difference.

The same criteria for time and space are applied for the AMSR2 and ATMS-measured TBs to construct the data collocated with the radiosonde observations. About 10% of radiosonde observations were discarded because of larger footprints of ATMS measurements particularly located near the scan edge. Note that all zenith angles of ATMS measurements collocated with the MOSAiC path crossing the central Arctic north of 85° are greater than 35° because the ATMS is on board the Sun-synchronous satellite with an orbital inclination of 98.79° (Figure S1).

Overall, a total of 418 sets of simulated snow/ice physical parameters, ERA atmospheric profiles, AMSR2 TBs, ATMS TBs and TELSEM2-based surface emissivities collocated with radiosonde observations are constructed. Any errors that stemmed from the mismatch of location caused by radiosonde drift and the mismatch of collocation time caused by radiosonde ascent are treated as a representation error to be included as a part of the observation error.

3 | IMPLEMENTATION OF EXPLICIT METHOD

Fundamentally, the explicit method retrieves multi-spectral emissivities and emitting layer temperatures (i.e. surface radiative boundary conditions) with information and constraints from the thermodynamic growth model and radiative transfer model for the snow and ice. In addition, we use information from the AMSR2 measurements for determining the snow/ice optical properties.

The overall procedures consist of two steps: (1) determining the optical properties of snow and ice – see the Appendix for detailed explanations of optical properties that are used as inputs to the radiative transfer calculation for snow and ice – and (2) estimating the snow/ice emissivity and emitting layer temperature. The steps (1–2) involve all or some parts of radiative transfer calculation from the TOA to the snow top, from the snow top to the ice bottom, from the ice bottom to the snow top, and then from the snow top to the TOA. In this, two radiative transfer models are employed, that is, the Snow and Sea Ice Emission Model (SSIEM: Tonboe, 2010; Tonboe *et al.*, 2011) and Radiative Transfer for TOVS (RTTOV: Saunders *et al.*, 1999). The configurations of SSIEM are the same as for the Microwave Emission Model of Layer Snowpacks (MEMLS: Wiesmann and Mätzler, 1999; Mätzler, 2006) and are based on the six-flux theory to describe radiative transfer in snow/ice layers including absorption, emission, reflection, multiple volume scattering, and roughness effect at the surface such as snow/ice interface. Note that we apply this approach up to ~50 GHz temperature-sounding channels because the accuracy of the snow/ice emission model at higher frequencies than 90 GHz is not in full confidence yet.

The radiative transfer calculations in steps (1–2) involve the surface reflection of the downwelling radiance to the snow surface. Although there is evidence that the snow reflection is more like Lambertian type for high frequencies of 89–183 GHz (Harlow, 2009) and more or less for 50 GHz temperature-sounding channels (Bormann, 2022), it is not clear what specularity ratio should be used for taking Lambertian characteristics into account because of the seasonally and regionally varying nature of the snow surface. Because of that, for the time being, the specular assumption is employed. Nevertheless, since the ATMS viewing angles at selected ice targets are at large 35°–65° (Figure S1) and the difference between two reflections becomes negligible in cases approaching 55° (Mätzler, 2005), the assumed specular reflection may not induce significant errors. Note that for the AMSR2 as 55° conically scanning radiometer, the distinction between specular and Lambertian reflections should be insignificant.

Detail procedures of how the optical properties of snow and ice are determined and used for the estimates of the emissivity and emitting layer temperature from snow/ice physical parameters are described in the following subsections. The procedure of determining the optical properties includes the minimization of variance of simulated window channel TBs against observed TBs. Because 3 window channels of ATMS should not be enough for the optimization, we use 10 AMSR2 window channel measurements to conduct the proposed optimization with higher confidence.

3.1 | Determination of optical properties for snow/ice radiative transfer model

For running the snow/ice radiative transfer model, SSIEM, vertical profiles of optical properties of snow and ice

are needed. In this study, we introduce an optimization scheme from which each layer's optical properties of snow and ice can be determined from the simulated physical parameters of snow and ice. The optimization scheme is summarized as a flow chart in Figure 2. In order to find the optimized solutions, we introduce a cost function expressed as the sum of squared residuals (RSS) of the simulated TOA TBs against observed TBs at 10 AMSR2 window channels (i.e. 10.7, 18.7, 23.8, 36.5 and 89.0 GHz of V/H-pol), that is:

$$\mathrm{RSS} = \sum_{j=1}^{k} \left[\mathrm{TB}^{\mathrm{sim}}(j) - \mathrm{TB}^{\mathrm{obs}}(j)\right]^2, \quad (1)$$

where $\mathrm{TB}^{\mathrm{sim}}$ and $\mathrm{TB}^{\mathrm{obs}}$ are simulated TB and measured TB, respectively. The "j" represents the channel number, and "k" is the total number of channels employed in this optimization process. Here, the atmospheric contributions to surface and to TOA are available from the RTTOV model with given ERA5 monthly mean profile. Accurate specification of atmospheric profiles for counting atmospheric

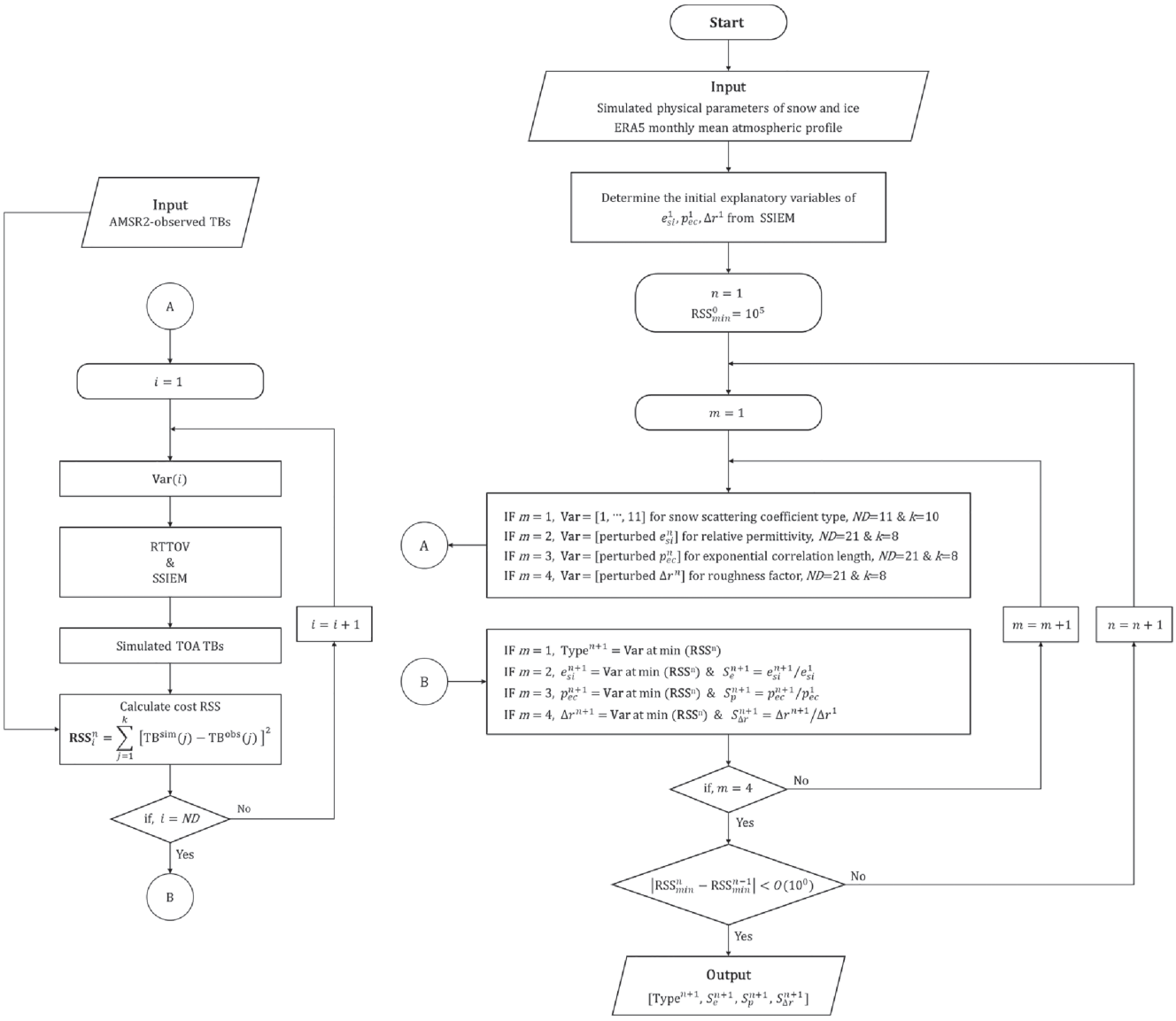

FIGURE 2 Flow chart of the optimization process employed in this study, which optimally determines the optimal optical properties of snow and ice [i.e. scattering type (Type), relative permittivity (e_{si}), exponential correlation length (p_{ec}), and roughness factor (Δr)]. The $\mathrm{TB}^{\mathrm{sim}}$ and $\mathrm{TB}^{\mathrm{obs}}$ are simulated brightness temperature (TB) and advanced microwave scanning radiometer-2 (AMSR2)-measured TB. The "S" means scale factor, and "m" and "n" are inner and outer loop iteration numbers for the minimization, respectively. The "i" represents the dimension counter linked to "ND" that indicates the number of perturbation dimension for the variable, while "j" and "k" denote the channel index and the total number of used channels, respectively

contributions may not be necessary for the determination of optical properties of snow and ice. It is because H_2O absorption is not much meaningful over the microwave window band especially under the very dry Arctic winter conditions, and O_2 absorption is also small over the microwave window band.

The employed optimal algorithm finds the solutions of multi-explanatory variables in an unconstrained nonlinear function, based on the Hooke–Jeeves method (Dutta, 2016). It takes a step in giving perturbations to variables in both negative and positive directions from an initial point and performs the model run called explanatory searching. Then, the algorithm finds a new point as the best guess if the minimum residual for perturbations is smaller than the old one. The search process continues in a series of these steps, and each step results in the cost function being smaller than the previous one. When the algorithm finds a new point whose residual is less than the predefined criteria, this point is regarded as the "solution." For the N-dimensional problem, the algorithm consists of a combination of N explanatory searching routines in turn.

The optimization procedures in this study are as follows. The ice scattering coefficient, relative permittivity (e_{si}), exponential correlation length (p_{ec}), and roughness factor (Δr) are initially determined at each snow/ice layer by the SSIEM with simulated profiles of physical parameters as input. Then, with the initial conditions, the snow scattering type is selected (out of 11 different parametrizations) for the snow volume scattering coefficients which yield the minimum RSS. Now, with a selected scattering type, the relative permittivity (e_{si}), exponential correlation length (p_{ec}), and roughness factor (Δr) are varied in turn. Here, instead of varying each layer's value individually, a scale factor is introduced so that a vertical profile for each optical property can be varied by simply applying the same scale factor to all layers. Each variation step given in the left side of Figure 2 finds values minimizing the cost function RSS. Note that for determining the snow scattering type $k = 10$ including 89 GHz, and for other optical properties $k = 8$ excluding 89 GHz. It is because 89 GHz channels are more sensitive to snow scattering than the other channels.

If the convergence criterion is not met, the nth iteration repeats with the newly selected snow scattering type, but with optical properties obtained at the $(n-1)$th iteration. It turned out that the first step of determining the snow scattering type largely determines the general features of the spectral distribution of AMSR2 TBs, and variations of the remaining three parameters appear to be secondary. Once the convergence criterion is met, the final profiles of optical properties are then considered to be the optimal conditions. As shown in the three-dimensional distribution of cost (Figure S2), for a given example of snow scattering type, the iteration of following three minimization

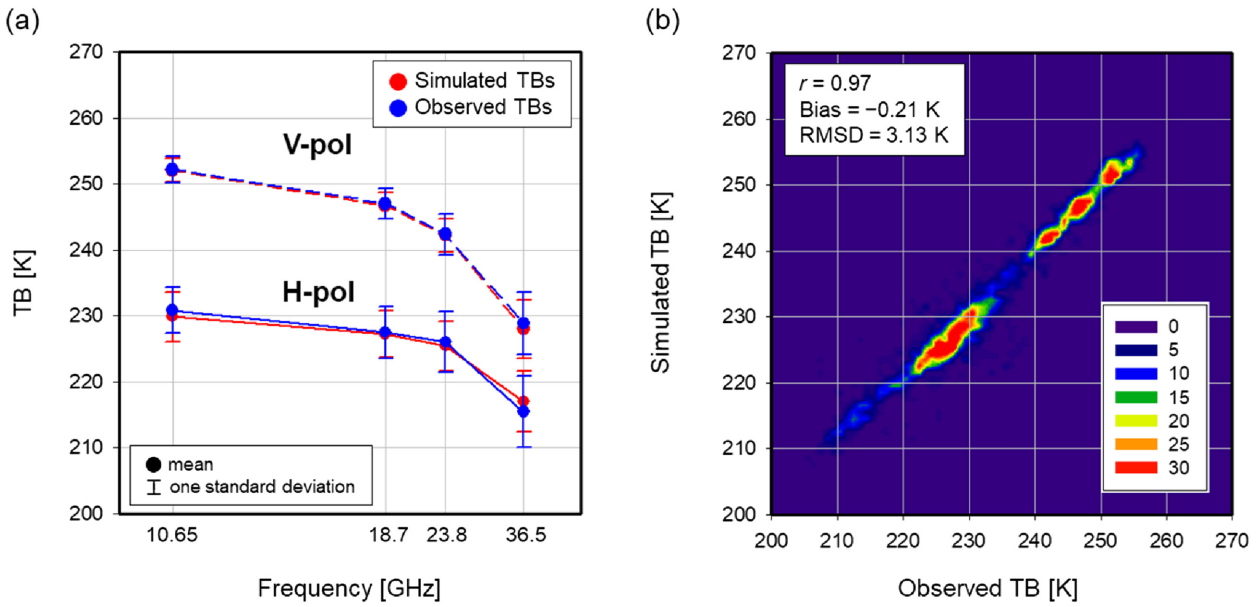

FIGURE 3 (a) Comparison of simulated top of the atmosphere (TOA) brightness temperatures (TBs) (red) against advanced microwave scanning radiometer-2 (AMSR2)-measured TBs (blue) along MOSAiC expedition track from 1 December 2019 to 31 March 2020 in terms of the mean and standard deviation at four channels for the vertical (dashed line) and horizontal (solid line) polarization. (b) Scatterplot of simulated TBs versus observed TBs across eight channels with correlation coefficient (r), mean deviation (bias), and root-mean-square deviation (RMSD). Colours in (b) represent number of data points [Colour figure can be viewed at wileyonlinelibrary.com]

steps can move the solutions toward the global minimum cost. After successfully finding the solution, the intrinsic scale factors for optical properties are kept for the drifting sea ice target until new AMSR2 observations are available.

The TB differences between simulated and observed TBs at AMSR2 channels may suggest how well the convergence was achieved for finding the optimized solutions. Figure 3 compares simulated TBs vs. observed TBs at AMSR2 eight channels (i.e. 10.7–36.5 of V/H-pol) at the final stage of the iteration process. It shows a correlation coefficient (r) of 0.97, a bias of −0.21 K, and a root-mean-square deviation (RMSD) of 3.13 K across eight channels nearly along the one-to-one line (Figure 3b), suggesting that the proposed optimization scheme can successfully provide the optical properties of snow and ice needed for running the SSIEM.

3.2 | Estimation of snow/ice emissivity and emitting layer temperature

In order to estimate the snow/ice emissivity and emitting layer temperature at the ATMS window and temperature-sounding channels, a surface radiative transfer calculation is conducted with the model-produced physical parameters and optimally determined optical properties of snow and ice. Note that the optimally determined optical properties are retrieved from AMSR2 window channel measurements.

To estimate the snow/ice emissivity, we run SSIEM twice, that is, with and without atmospheric downwelling radiance at the snow surface, for given snow/ice profiles of physical parameters and optical properties. In the case of with-downwelling radiance, any arbitrary value of the downwelling radiance ($N^{\downarrow}$) can be assigned. Since two runs give two different upwelling radiances at the surface (i.e. $N_o{}^{\uparrow}$ for without-downwelling radiance and $N_d{}^{\uparrow}$ for with-downwelling radiance), their difference ($\Delta N^{\uparrow} = N_d{}^{\uparrow} - N_o{}^{\uparrow}$) can be attributed to the reflected downwelling radiance back to the atmosphere, that is, $\Delta N^{\uparrow} = N^{\downarrow}(1-\varepsilon_i)$, and thus $\varepsilon_i = 1 - (\Delta N^{\uparrow}/N^{\downarrow})$. Once ε_i is estimated, the emitting layer temperature (T_e) can be retrieved, that is, $T_e = N_o{}^{\uparrow}/\varepsilon_i$.

It is of interest to examine how the lower boundary condition specified with estimated snow/ice emissivity and emitting layer temperature influences the TOA TB simulation. In doing so, we apply explicitly calculated surface radiative boundary conditions for simulating ATMS window channel TBs (i.e. 23.8 and 31.4 GHz) and compare them with ATMS measurements. The assumption is that ATMS window channel TBs should be simulated well if the surface boundary conditions are accurate enough. In other words, if simulated TBs show large discrepancies from measured TBs, then it should be difficult to use the estimated parameters for any type of application. For ATMS TB simulation, the following emissivity conversion is applied because ATMS measures TB in Quasi-Vertical and Quasi-Horizontal (i.e. QV and QH) polarizations (Weng *et al.*, 2013):

$$\varepsilon_{\mathrm{QV(or\ QH)}} = \varepsilon_{\mathrm{V(or\ H)}}\cos^2\theta + \varepsilon_{\mathrm{H(or\ V)}}\sin^2\theta, \qquad (2)$$

where θ is satellite viewing angle.

TB simulation is done using the atmospheric profiles of ERA5 reanalysis along the MOSAiC expedition track with the physically estimated emissivity and emitting layer temperature. We also simulate the ATMS window channel TBs but with TELSEM2-derived emissivity and ERA5 skin temperature. In this TELSEM2-related simulation, the surface emissivity should be associated with the skin temperature, not with the emitting layer temperature. The scatterplot of observed TBs versus simulated TBs and the histogram of their TB departures are shown in Figure 4. It is shown that simulated TBs from the explicit method are in good agreement with the observed TBs, with correlation coefficients of 0.98 and 0.96, biases of −1.58 and −3.02 K, and standard deviations of 1.24 and 1.72 K for 23.8 and 31.4 GHz QV-pol channels, respectively. Both channels show strong linear relationships between the simulated and observed TBs, and distributions of the TB departure show a well-shaped Gaussian distribution without significant skewness. These results strongly suggest that the explicit method is capable of providing the lower boundary condition of the atmospheric radiative transfer for the successful ATMS window channel simulation.

On the other hand, TELSEM2-derived surface emissivity resulted in substantial departures from the one-to-one corresponding line despite being based on ERA5 skin temperature; departures (observation minus simulation) are ~15 K on average and mostly positive. Furthermore, TB departures show large standard deviations. This result may reflect a cautionary note that the TELSEM2-generated monthly emissivity has not been fully conclusive for the sea ice area (Wang *et al.*, 2017).

4 | SET-UP FOR 1D-VAR EXPERIMENT

In order to examine how the proposed approach improves temperature retrieval from microwave measurements, estimated snow/ice emissivity and emitting layer temperature are incorporated into the NWP SAF 1D-Var-v1.2 standalone system (Havemann, 2020). Figure 5 shows the

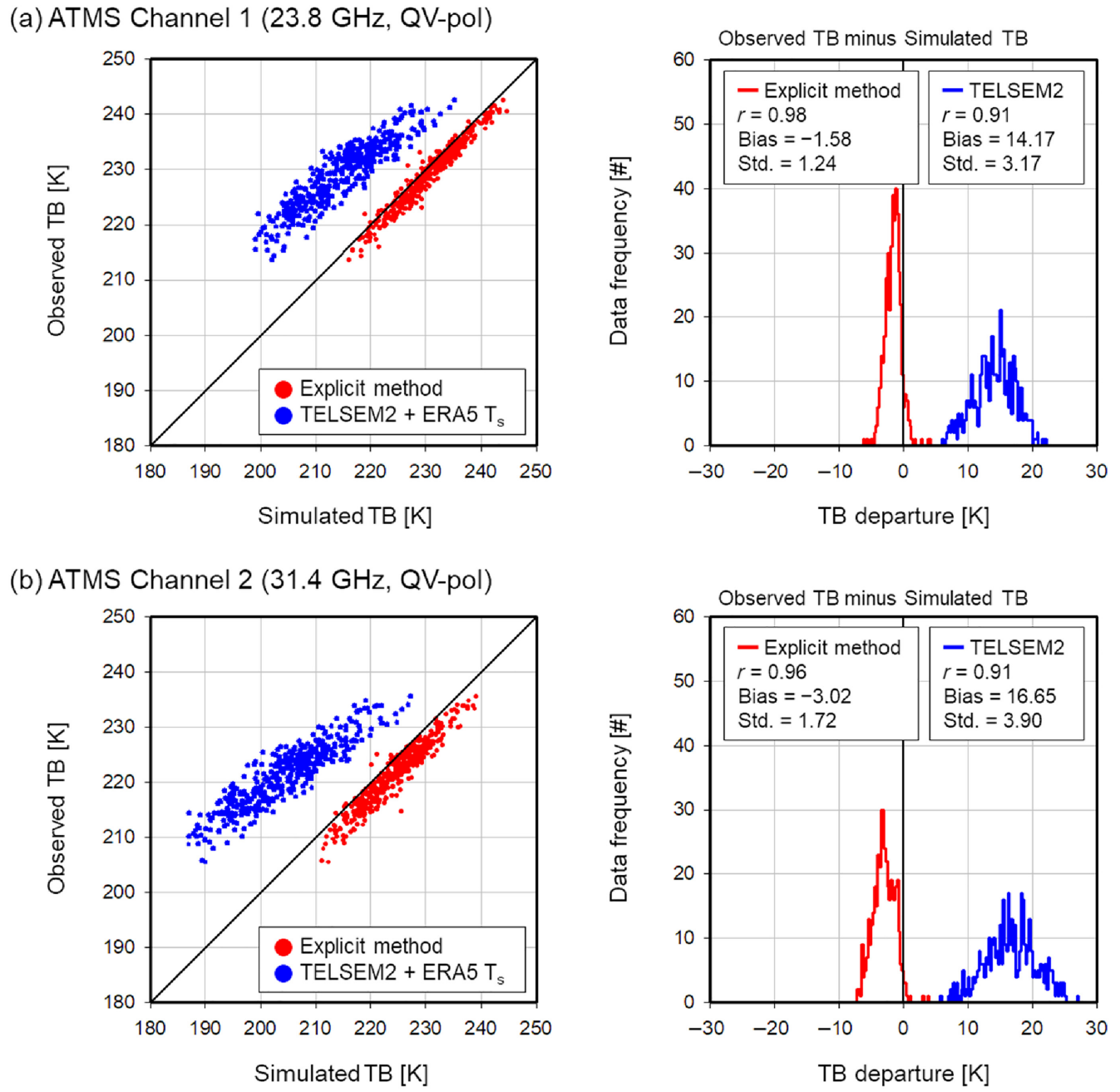

FIGURE 4 (left) Scatterplots of observed TBs versus simulated TBs at advanced technology microwave sounder (ATMS) (a) 23.8 GHz and (b) 31.4 GHz QV-pol channels, and (right) associated data frequency distribution for the brightness temperature (TB) departures of simulated TBs from observed TBs [Colour figure can be viewed at wileyonlinelibrary.com]

schematic diagram of the 1D-Var system. In this procedure, 1D-Var minimizes the cost function J(**x**) given as follows:

$$\mathrm{J}(\mathbf{x}) = \frac{1}{2}(\mathbf{x}-\mathbf{x}_\mathrm{b})^\mathrm{T}\,\mathbf{B}^{-1}\,(\mathbf{x}-\mathbf{x}_\mathrm{b}) + \frac{1}{2}\left\{\mathbf{y}_\mathrm{o}-H(\mathbf{x})\right\}^\mathrm{T}\mathbf{R}^{-1}\left\{\mathbf{y}_\mathrm{o}-H(\mathbf{x})\right\}, \quad (3)$$

where $\mathbf{x}$ is the control variable, $\mathbf{x}_\mathrm{b}$ is the background variable, and $\mathbf{y}_\mathrm{o}$ is the observed radiance at the given sensor channels. $\mathbf{B}$ is the background error covariance matrix associated with background variable $\mathbf{x}_\mathrm{b}$. $\mathbf{R}$ is the observation error covariance matrix constructed from available error sources including instrumental error, forward modelling error, surface boundary modelling error, and other errors related to the data processing (Janjić *et al.*, 2018). The superscript "T" denotes the matrix transpose, and $H(\mathbf{x})$ is the forward-modelled radiance in which H is the RTTOV model. Given that the cloud-affected signal to the microwave radiative transfer over sea ice is typically much

smaller than the surface signal (Bormann, 2022), we perform the 1D-Var with clear-sky assumption without cloud screening.

For the 1D-Var experiment, as schematically depicted in Figure 5, background and observation error covariances (**B** and **R**) are needed, and we construct **B** and **R**, which are linked to the background and observation fields ($\mathbf{x}_b$ and $\mathbf{y}_o$) with non-bias against the "true" state ($\mathbf{x}_t$). Because of its unbiased condition and correctly known **B** and **R**, we can call this experiment "ideal." For generating **B** and **R**, as summarized in Figure 6, we follow the method described in Bouttier and Courtier (2002). Here, the error states of background and observation ($\mathbf{e}_b$ and $\mathbf{e}_o$) are defined using the true state, that is:

$$[\mathbf{e}_b] = \mathbf{x}_b - [\mathbf{x}_t], \tag{4}$$

$$[\mathbf{e}_o] = [\mathbf{y}_o] - H([\mathbf{x}_t]), \tag{5}$$

where the bracket symbol [] is a matrix containing the total 418 radiosonde observations, and H is the forward model operator constrained with model-generated surface boundary conditions. Consequently, each error covariance matrix can be written as follows:

Background error covariance **B**

$$= \overline{\left([\mathbf{e}_b] - \overline{\mathbf{e}_b}\right)\left([\mathbf{e}_b] - \overline{\mathbf{e}_b}\right)^T}, \tag{6}$$

Observation error covariance **R**

$$= \overline{\left([\mathbf{e}_o] - \overline{\mathbf{e}_o}\right)\left([\mathbf{e}_o] - \overline{\mathbf{e}_o}\right)^T}, \tag{7}$$

where $\overline{\mathbf{e}_b}$ and $\overline{\mathbf{e}_o}$ are mean values of $[\mathbf{e}_b]$ and $[\mathbf{e}_o]$.

With obtained errors for background and observation states, this ideal experiment is designed to demonstrate that the use of surface-sensitive microwave channels for 1D-Var retrieval is possible with model-produced emissivity and emitting layer temperature. The successful retrieval is considered the prerequisite for applications such as data assimilation including surface-sensitive microwave channels. In the following subsections, we provide how this ideal experiment is set up.

4.1 | "True" atmospheric state

In this study, the "true" state of the atmospheric profiles refers to an ideal state that is perfectly linked to $\mathbf{x}_b$ and $\mathbf{y}_o$ with **B** and **R**. The true state is constructed by combining

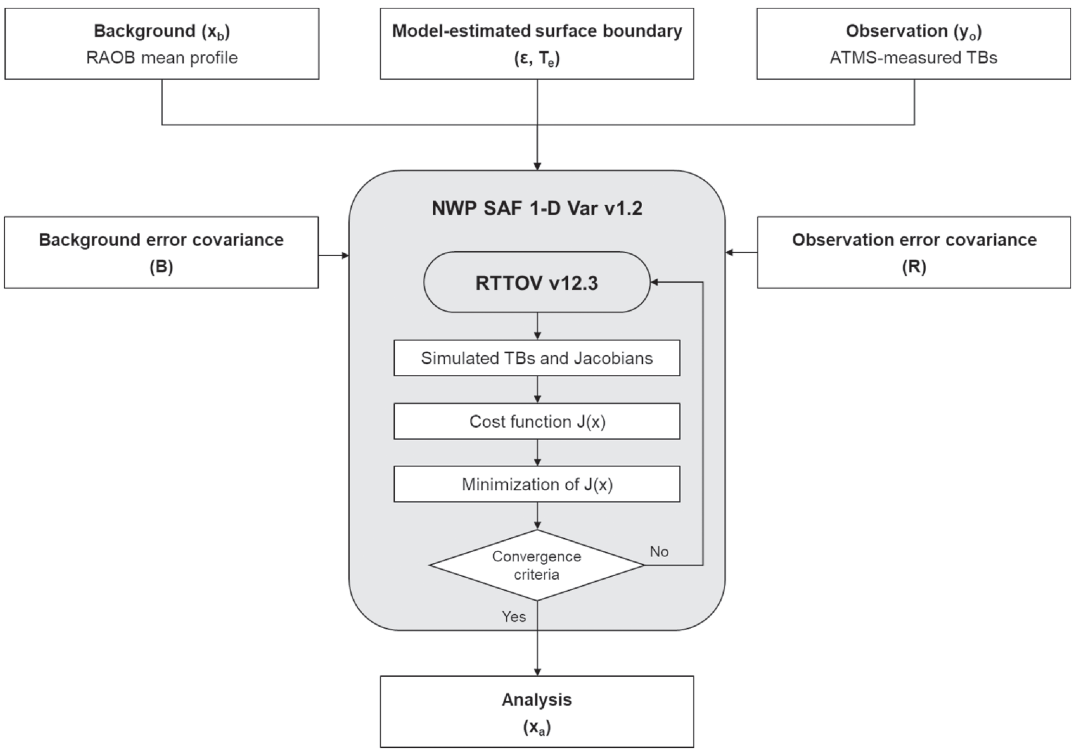

FIGURE 5 Schematic diagram of the 1D-Var experiment. A grey box indicates the numerical weather prediction (NWP) SAF 1D-Var standalone system, including the RTTOV model

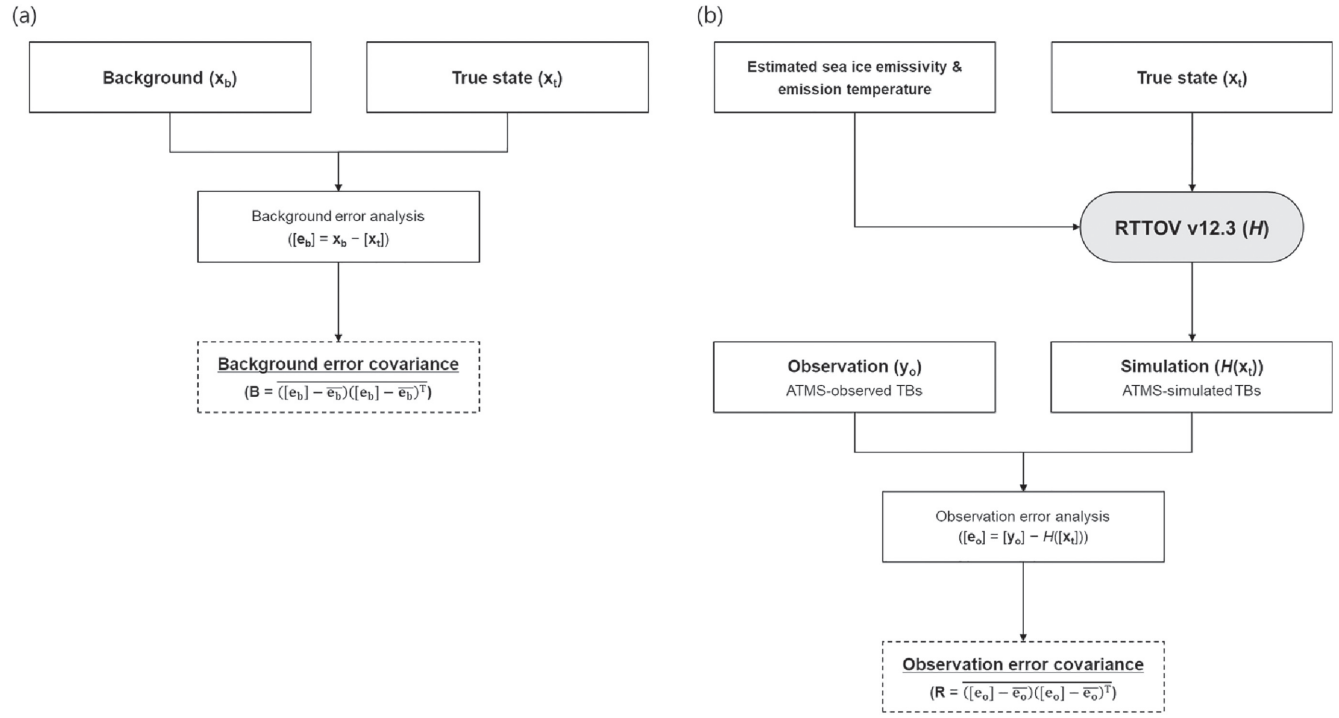

FIGURE 6 Schematic diagram of constructing (a) background and (b) observation error covariance matrices. A grey box indicates the RTTOV (Radiative Transfer for TOVS) model

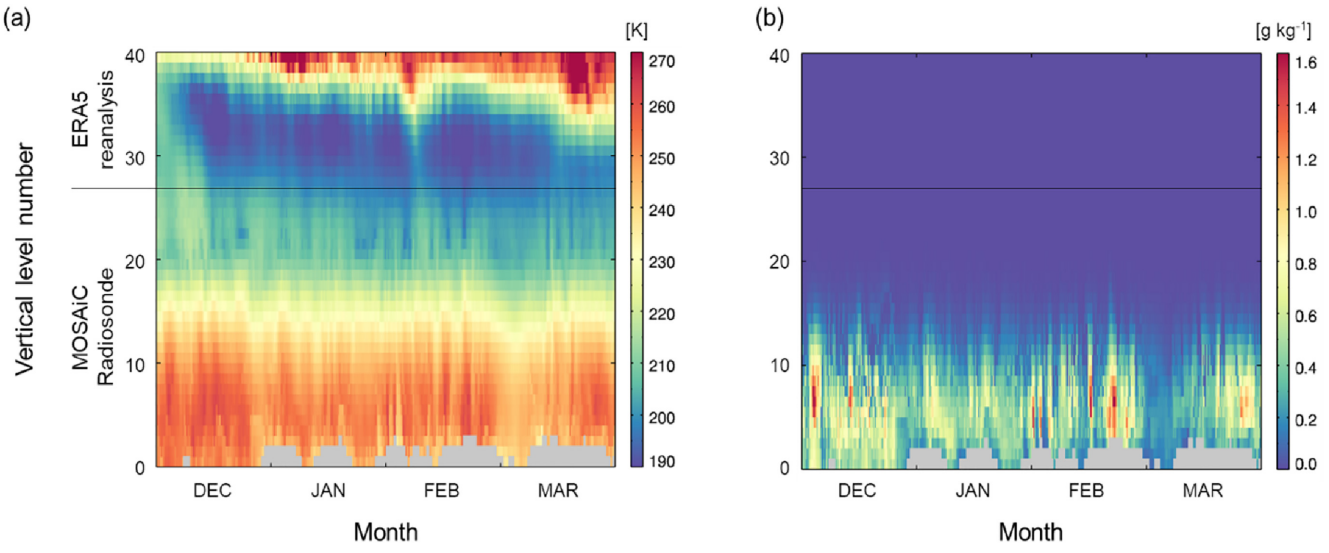

FIGURE 7 Cross-sections of (a) temperature (K) and (b) water vapour (specific humidity in units of g·kg^{-1}) profiles of the constructed true state along the multidisciplinary drifting observatory for the study of Arctic climate (MOSAiC) expedition track during the analysis period from 1 December 2019 to 31 March 2020 [Colour figure can be viewed at wileyonlinelibrary.com]

MOSAiC radiosonde observations with ERA5 reanalysis data. It is because the balloon-borne radiosonde measures generally up to the lower part of the stratosphere, and thus it cannot provide the full temperature and humidity profile up to about 1 hPa, which is needed for running the 1D-Var system. Furthermore, the highest data level varies with each radiosonde measurement. Thus, the profile below 100 hPa level is from MOSAiC radiosonde observations while above 100 hPa level it is from ERA5 reanalysis data.

The time series of constructed true state of temperature and humidity profiles along the MOSAiC trajectory

over the period from 1 December 2019 to 31 March 2020 is given in Figure 7. The number of vertical levels is 40, all of which are mandatory levels for the 1D-Var system. The horizontal line in the diagram separates the data used for constructing the profile for the true state. It indicates that there is no obvious discontinuity across the data boundary in both temperature and humidity fields.

4.2 | Observation state (y_o) and error covariance (R)

The observation state represents ATMS-measured tropospheric temperature-sounding channel TBs (nos. 4–10; see Table 2 for their respective frequencies); thus, the dimension of $\mathbf{y}_o$ is 7. The Jacobians for ATMS channel nos. 4–10 are shown in Figure 8, and ATMS channel nos. 4–6 are defined as surface-sensitive channels because they are influenced by the surface boundary, unlike channel nos. 7–10. Here, we quantify and remove the biases in the observation state and then define the observation error variances for the 1D-Var process.

For the bias correction of observed TBs, we adopt a linear predictor depending on the satellite viewing angle, that is:

$$b(j,\theta) = \overline{([y_o(j,\theta)] - [H(\boldsymbol{x}_t, j, \theta)])}, \tag{8}$$

$$\left[y'_o(j,\theta)\right] = [y_o(j,\theta)] - b(j,\theta), \tag{9}$$

where b is the bias given as a function of the satellite viewing angle θ, j is the channel number (i.e. $j=4$, 5 or 6), and y_o and y'_o are observed and bias-corrected TBs, respectively. Since the true state is used as input to the radiative transfer model (H; RTTOV model used for 1D-Var) constrained with model-generated surface boundary, the forward-modelled state vector $H(\boldsymbol{x}_t)$ is considered to be the true-based TB simulation. This implies that the observation systematic errors can be treated as an error including instrumental error, forward modelling error, surface boundary modelling error, and others related to the data processing (such as mismatching time and location between radiosonde observation and satellite measurement).

Scatterplots of simulated TBs vs. observed TBs for three channels (nos. 4–6), frequency distributions of TB departures (observation minus simulation) and their associated scan angle dependence are shown in Figure 9. Before the bias correction, the observed TBs show biases of −0.89, −0.80 and −0.18 K for channel nos. 4–6 against simulated TBs, with respective standard deviations of 0.88, 0.37 and 0.24 K. The scan angle dependence for the TB departure distribution is clear.

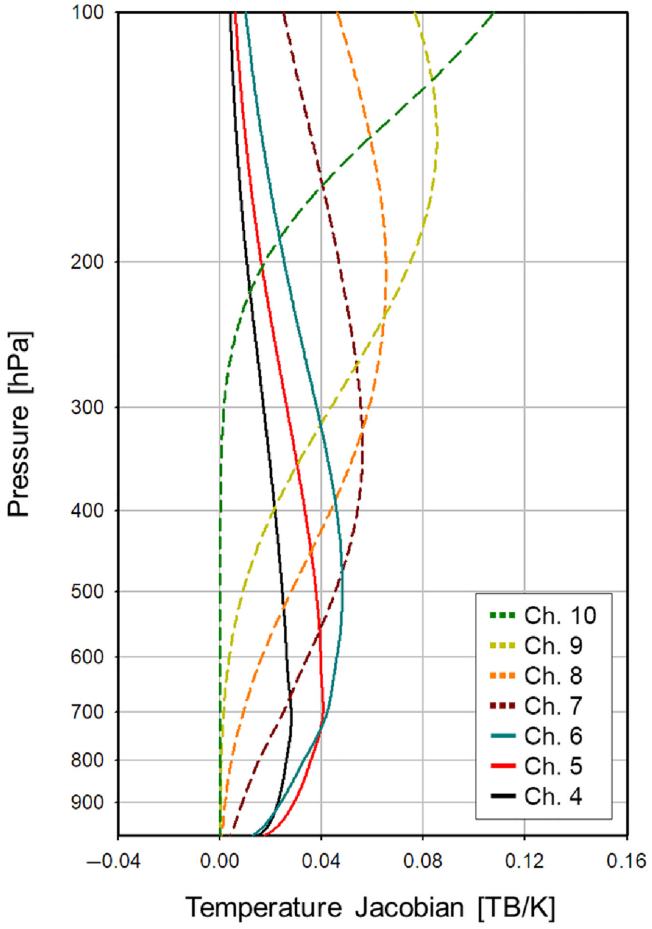

FIGURE 8 Temperature Jacobians, computed for the mean atmosphere of the true state, for the tropospheric temperature-sounding channels 4–10 of the advanced technology microwave sounder (ATMS) sensor [Colour figure can be viewed at wileyonlinelibrary.com]

Compared to the "before the correction," the bias correction across incident angles brought into reduced standard deviations of 0.50, 0.26 and 0.23 K for ATMS channel nos. 4–6, respectively. At the same time, the TB departure distributions indicates that the bias correction turns TB departures into more of the Gaussian distribution (given in red colour in the second panels). Also clear is the distribution nearly independent of the scan angles after the correction (given in red colour in the third panels). Thus, after applying the observation bias correction, the observation state of TBs shows a Gaussian-type random distribution with a non-bias and non-scan angle dependence.

We also estimated observation biases for other ATMS temperature-sounding channels (i.e. channel nos. 7–10) by applying the same bias correction procedures (results are not shown). Since these channels are presumably not affected by the surface conditions (as shown in Figure 8), our developed scheme does not apply for these channels. After removing the respective observation

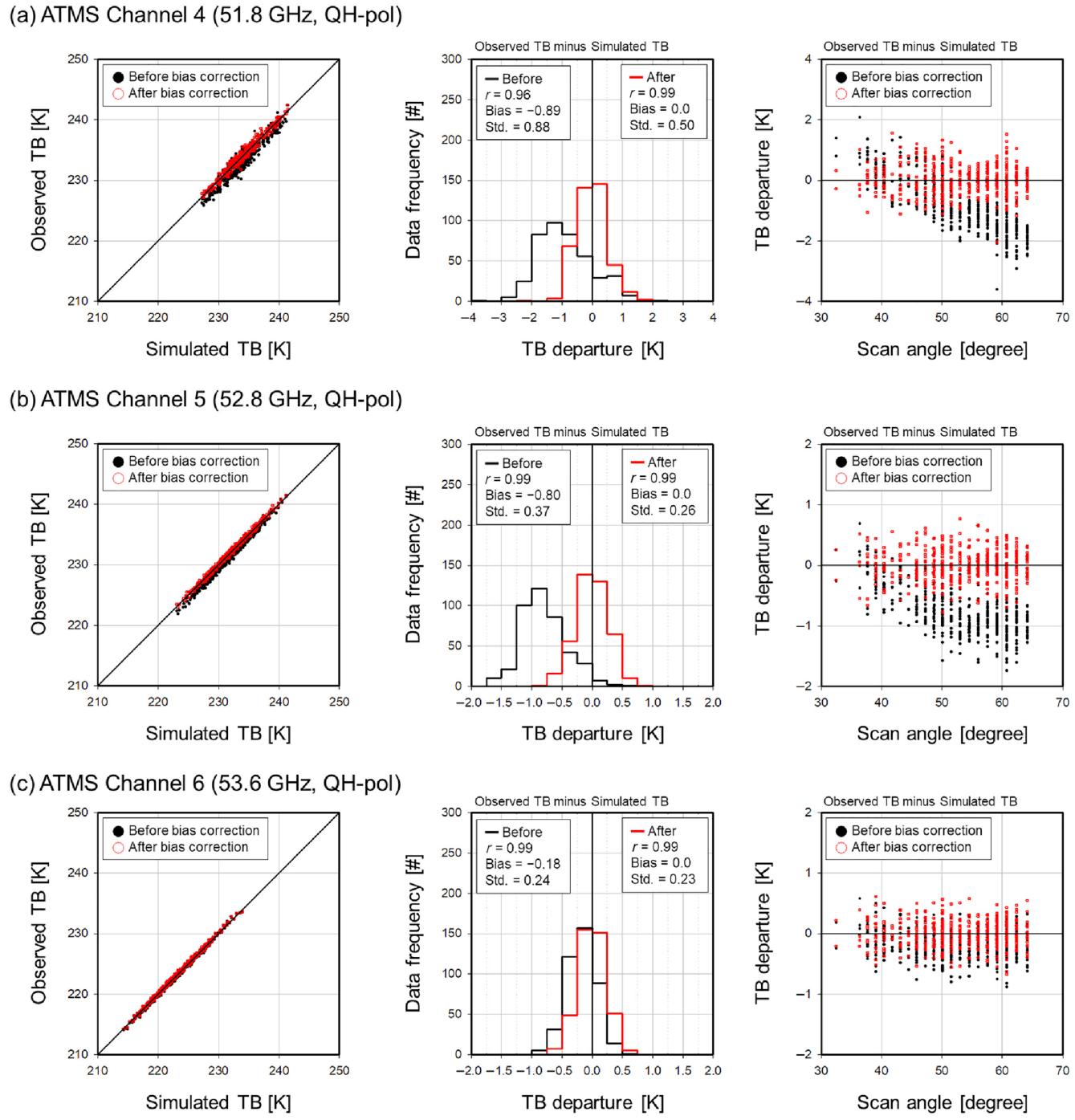

FIGURE 9 (left) Scattergram of simulated TBs versus observed TBs, (middle) frequency distribution of the difference between two brightness temperature (TB) sets, and (right) frequency distribution of the difference between two TB sets given at scan angles at advanced technology microwave sounder (ATMS) (a) 51.8 GHz QH-pol, (b) 52.8 GHz QH-pol, and (c) 53.6 GHz QH-pol channels. Black and red indicate "before" and "after" the viewing angle bias correction, respectively [Colour figure can be viewed at wileyonlinelibrary.com]

biases, the observation states for these channels are also obtained.

The bias-corrected ATMS TBs are used as the observation state for the 1D-Var experiment. Then, the observation random errors are exactly calculated from the known true state (Equations 5 and 7), and their variances are a diagonal component of the observation error covariance matrix **R**. Each channel measurement is assumed to be independent of others so that other covariance terms are assumed to be zero. The magnitudes of diagonal component of the new **R** matrix for channel nos. 4–10 are given in Figure 10, together with error magnitudes of the

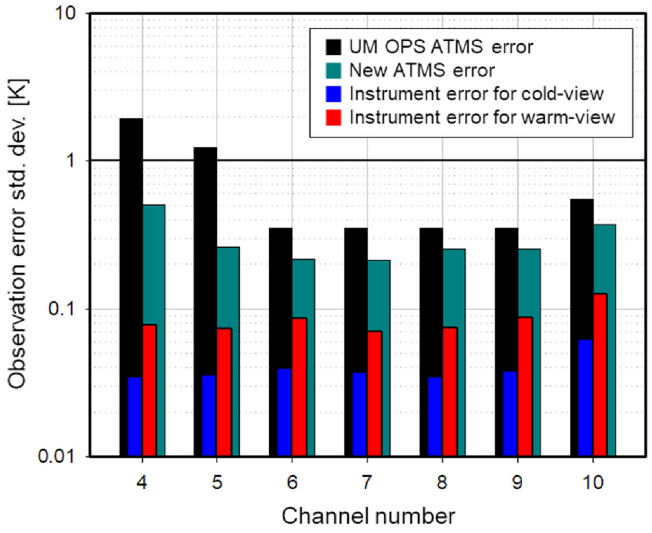

FIGURE 10 Diagonal components of the UM OPS advanced technology microwave sounder (ATMS) R matrix (black bars) and new ATMS R matrix (cyan bars) for temperature-sounding channels 4–10, along with instrument errors for internal warm load and deep space cold calibration targets (blue and red bars). Error magnitude in the *y*-axis is given in a logarithmic scale [Colour figure can be viewed at wileyonlinelibrary.com]

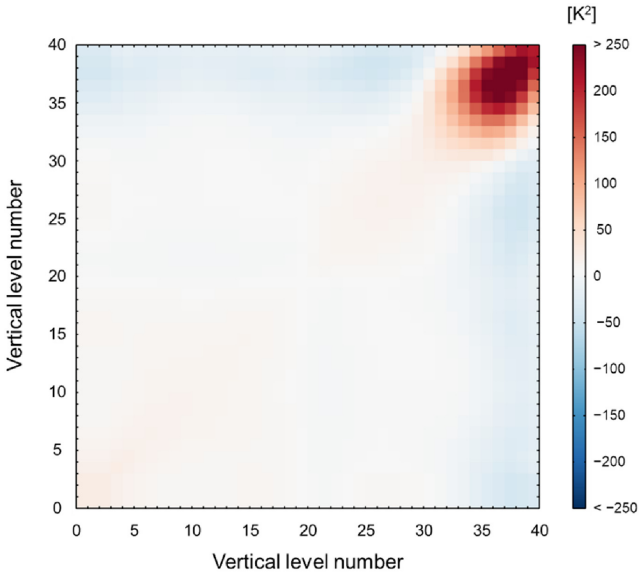

FIGURE 11 Background error covariance matrix calculated by errors between the mean temperature profile and the true temperature profiles. The level numbers of *x*- and *y*-axes are in the order from surface to top of the atmosphere (TOA) as in Figure 7 (not level numbers prescribed by the 1D-Var) [Colour figure can be viewed at wileyonlinelibrary.com]

UK Met Office Unified Model (UM) Observation Processing System (OPS) **R** matrix and ATMS instrument noise. Note again that observation random errors are composed of instrumental error, forward modelling error, surface boundary modelling error, and others related to the data processing. Here, since errors associated with the instrument and forward operator are the same in both, it is suggested that the differences are due to the surface boundary and processing errors. If the processing errors are minor to count, the error differences likely come from uncertain surface boundary conditions. In Figure 10, the exceptionally smaller errors are found in more surface-sensitive channel nos. 4–5, implying that these error reductions are due to more accurate surface boundary conditions, and thus, it may assure this approach is in the right direction.

4.3 | Background state ($\mathbf{x_b}$) and error covariance (B)

For the background state of temperature ($\mathbf{x}_b$), we use the mean temperature profile of the true state; thus, the dimension of $\mathbf{x}_b$ is 40. Moreover, the background state holds unbiased conditions against the true state. The background error covariance matrix **B** is constructed from Equations (4) and (6), and the resultant **B** matrix is shown in Figure 11. The humidity field is not a control variable but a fixed field as true state throughout the 1D-Var experiment.

5 | RETRIEVAL EXPERIMENTS AND RESULTS

In order to examine whether the use of estimated snow/ice emissivity and emitting layer temperature makes it possible to use the surface-sensitive microwave measurements for applications such as data assimilation, we take 1D-Var temperature retrieval from ATMS temperature-sounding channels. The successful retrieval can be counted as the prerequisite for other in-depth applications involving surface-sensitive channels. Two retrieval experiments are conducted: retrievals (1) from the use of surface-insensitive channels, that is, channel nos. 7–10 (referred to as the "control" experiment) and (2) from all sounding channels (nos. 4–10) including surface-sensitive channels (nos. 4–6) (referred to as the "surface" experiment).

Retrieval is done using the 1D-Var system for given ATMS TBs. The results are compared with the true state to assess how well the mean temperature profile (i.e. background) is restored to its original true state. Because there are 418 true profiles and corresponding ATMS TBs, results are given in terms of bias and root-mean-square error (RMSE) of retrieved profiles against true profiles

(Figure 12). Results indicate that there seem to be no meaningful biases arisen from the 1D-Var approach in both "control" and "surface" experiments. On the other hand, both experiments show a significant reduction of RMSEs, compared to RMSEs of the background field. When "control" and "surface" experiments are compared, the surface experiment clearly demonstrates that a significant improvement can be made in the lower tropospheric layers below about 500 hPa level, from the additional use of surface-sensitive channels. Improvements are largest over the 850–950 hPa layer. Overall, the current attempt to use explicitly determined snow/ice emissivity and emitting layer temperature as a constraint of the surface radiative boundary condition brought in the successful use of surface-sensitive channel measurements in the 1D-Var retrieval.

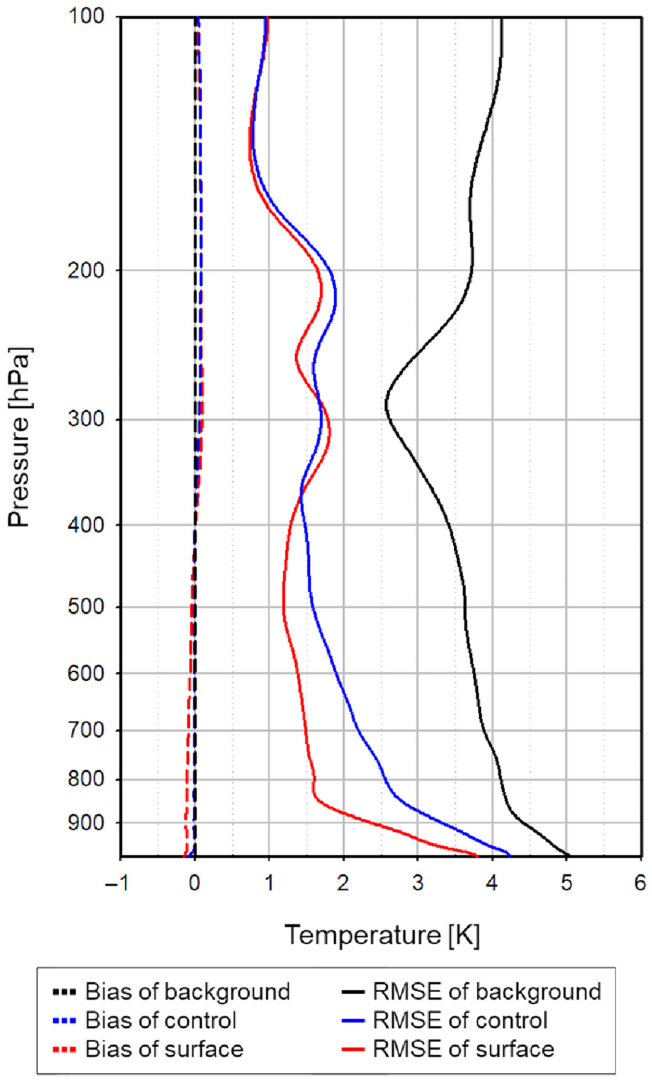

FIGURE 12 Biases (dashed line) and RMSEs (solid line) of the temperature profiles against the true state. The results of the control experiment (blue) and the surface experiment (red) are given together with the background (black) [Colour figure can be viewed at wileyonlinelibrary.com]

6 | CONCLUSIONS AND DISCUSSION

We propose an explicit method of estimating the surface radiative boundary conditions (namely emissivity and emitting layer temperature of snow and ice) over the Arctic sea ice region during winter. The method determines optimal snow/ice optical properties (i.e. snow scattering type, relative permittivity, exponential correlation length, and roughness) from model-produced snow/ice physical parameters (i.e. snow/ice depths and vertical distributions of temperature, density, salinity, and grain size) and AMSR2-measured TBs. Subsequently, the emissivity and emitting layer temperature of snow and ice are estimated from explicit surface radiative transfer calculation using physical parameters and optical properties within the snow and ice layers.

In order to examine whether this approach can help to use the surface-sensitive microwave channel measurements over the Arctic sea ice region for the data assimilation, the 1D-Var temperature retrievals were performed with the ATMS temperature-sounding channels along the trajectory of the MOSAiC expedition from 1 December 2019 to 31 March 2020. Successful retrieval is thought to be the prerequisite for the use. In preparing 1D-Var experiments, the simulated TBs for the ATMS window channels with the use of the ERA5 atmospheric profiles and explicitly calculated surface boundary conditions were compared with observed TBs. It was shown that simulated and observed TBs are close to the one-to-one line, and the TB differences follow a well-shaped Gaussian distribution. The close agreement between simulated and observed TBs strongly suggests that the explicit method proposed in this study provides the snow/ice emissivity and emitting layer temperature, which then can successfully describe the lower boundary condition needed for atmospheric radiative transfer calculation.

We further conducted the ideal 1D-Var experiments to examine how the inclusion of surface-sensitive ATMS channels (nos. 4–6) using the explicitly estimated surface boundary conditions can give positive influences on temperature retrieval. Results demonstrate that the use of surface-sensitive channel measurements can significantly improve temperature retrieval, especially in the lower troposphere (500 hPa to surface). We argue that without an accurate prescription of surface boundary conditions, a simple addition of surface-sensitive channels cannot guarantee the retrieval itself. Better retrieval is thought to be possible not only because of added new channels but

also because of accurate surface information. Considering that successful retrieval should be the prerequisite for the active use of surface-sensitive microwave measurements, the results suggest that useful information for potential applications to assimilation can be drawn from surface-sensitive microwave-sounding channel TBs over the Arctic sea ice surface.

We note that this prospect is for the wintertime only. In order to apply this approach for the melting season, first, the melting processes should be included in the thermodynamic model. Other challenges, such as the radiative transfer under the conditions of wet snow and melt ponds, should be taken to achieve the summertime applications. In addition, the capability to calculate the snow/ice radiative transfer at higher frequencies, including water vapour bands around ~183 GHz, should be improved for the successful implementation of the proposed explicit method.

AUTHOR CONTRIBUTIONS

Eui-Jong Kang: Conceptualization; data curation; formal analysis; investigation; methodology; software; validation; visualization; writing – original draft; writing – review and editing. **Byung-Ju Sohn:** Conceptualization; funding acquisition; methodology; supervision; writing – original draft; writing – review and editing. **Rasmus Tage Tonboe:** Conceptualization; methodology; writing – review and editing. **Young-Chan Noh:** Methodology; writing – review and editing. **In-Hyuk Kwon:** Project administration; writing – review and editing. **Sang-Woo Kim:** Funding acquisition; resources; writing – review and editing. **Marion Maturilli:** Data curation; writing – review and editing. **Hyun-Cheol Kim:** Data curation; writing – review and editing. **Chao Liu:** Writing – review and editing.

ACKNOWLEDGEMENTS

The authors express their sincere thanks to two anonymous reviewers who provided much valuable discussion and insight on how this article can be improved. This work was carried out through the R&D project on the Development of a Next-generation Data Assimilation System of the Korea Institute of Atmospheric Prediction Systems (KIAPS) funded by the Korea Meteorological Administration (KMA) (No. KMA2020-02211). Part of this work was supported by the National Research Foundation of Korea (NRF) grant funded by the Korea government (MSIT) (No. NRF-2021R1A4A5032320). R. T. Tonboe was supported by the ESA project: Performance Evaluation of Arctic Weather Satellite Data (No. 4000136511/21/NL/IA), and Y.-C. Noh was supported by Korea Polar Research Institute (KOPRI) grant funded by the Ministry of Oceans and Fisheries (No. KOPRI PE23010). Radiosonde data used in this article were produced as part of the international Multidisciplinary drifting Observatory for the Study of the Arctic Climate (MOSAiC) with the tag MOSAiC20192020 (AWI_PS122_00), and were obtained through a partnership between the leading Alfred Wegener Institute (AWI), the Atmospheric Radiation Measurement (ARM) User Facility, a US Department of Energy facility managed by the Biological and Environmental Research (BER) Program, and the German Weather Service (DWD).

FUNDING INFORMATION

R&D project on the Development of a Next-generation Data Assimilation System of the Korea Institute of Atmospheric Prediction Systems (KIAPS) funded by the Korea Meteorological Administration (KMA). Grant Number: KMA2020-02211. National Research Foundation of Korea (NRF) grant funded by the Korea government (MSIT). Grant Number: NRF-2021R1A4A5032320.

ORCID

Byung-Ju Sohn https://orcid.org/0000-0001-6134-3515
Hyun-Cheol Kim https://orcid.org/0000-0002-6831-9291

REFERENCES

Bauer, P., Magnusson, L., Thépaut, J.N. and Hamill, T.M. (2016) Aspects of ECMWF model performance in polar areas. *Quarterly Journal of the Royal Meteorological Society*, 142(695), 583–596. https://doi.org/10.1002/qj.2449.

Bauer, P., Thorpe, A. and Brunet, G. (2015) The quiet revolution of numerical weather prediction. *Nature*, 525(7567), 47–55. https://doi.org/10.1038/nature14956.

Bormann, N. (2022) Accounting for Lambertian reflection in the assimilation of microwave sounding radiances over snow and sea-ice. *Quarterly Journal of the Royal Meteorological Society*, 148(747), 2796–2813. https://doi.org/10.1002/qj.4337.

Bormann, N., Lupu, C., Geer, A., Lawrence, H., Weston, P. and English, S. (2017) *Assessment of the Forecast Impact of Surface-Sensitive Microwave Radiances over Land and Sea-Ice*. Reading, UK: European Centre for Medium Range Weather Forecasts (ECMWF) Retrieved from https://www.ecmwf.int/en/elibrary/17674-assessment-forecast-impact-suface-sensitive-microwave-radiances-over-land-and-sea.

Bouttier, F. and Courtier, P. (2002) *Data Assimilation Concepts and Methods*. Reading: European Centre for Medium Range Weather Forecasts (ECMWF) Retrieved from https://www.ecmwf.int/en/elibrary/79860-data-assimilation-concepts-and-methods.

Day, J.J., Sandu, I., Magnusson, L., Rodwell, M.J., Lawrence, H., Bormann, N. and Jung, T. (2019) Increased Arctic influence on the midlatitude flow during Scandinavian blocking episodes. *Quarterly Journal of the Royal Meteorological Society*, 145(725), 3846–3862. https://doi.org/10.1002/qj.3673.

Debye, P., Anderson, H.R. and Brumberger, H. (1957) Scattering by an inhomogeneous solid. II. The correlation function and its application. *Journal of Applied Physics*, 28(6), 679–683. https://doi.org/10.1063/1.1722830.

Dutta, S. (2016) *Optimization in Chemical Engineering*. Cambridge: Cambridge University Press.

Dybkjær, G., Eastwood, S., Pfeiffer, R. and Howe, E. (2018) *OSI SAF High Latitudes L2 Sea and Sea Ice Surface Temperature Product User Manual (OSI-205-a/b)*. Paris: Ocean and Sea Ice Satellite Application Facility Retrieved from http://osisaf.met.no/docs/osisaf_cdop3_ss2_pum_hl-l2-sst-ist_v1p3.pdf.

Frankenstein, G. and Garner, R. (1967) Equations for determining the brine volume of sea ice from −0.5° to −22.9°C. *Journal of Glaciology*, 6(48), 943–944. https://doi.org/10.3189/S0022143000020244.

Harlow, R.C. (2009) Millimeter microwave emissivities and effective temperatures of snow-covered surfaces: evidence for Lambertian surface scattering. *IEEE Transactions on Geoscience and Remote Sensing*, 47(7), 1957–1970. https://doi.org/10.1109/TGRS.2008.2011893.

Havemann, S. (2020) *NWPSAF 1D-Var User Manual (Version 1.2)*. European Organization for the Exploitation of Meteorological Satellites (EUMETSAT) Numerical Weather Prediction (NWP) Satellite Application Facilities (SAF) Retrieved from https://nwp-saf.eumetsat.int/site/software/1d-var/documentation/1dvar-user-guide/.

Hersbach, H., Bell, B., Berrisford, P., Hirahara, S., Horányi, A., Muñoz-Sabater, J., Nicolas, J., Peubey, C., Radu, R., Schepers, D., Simmons, A., Soci, C., Abdalla, S., Abellan, X., Balsamo, G., Bechtold, P., Biavati, G., Bidlot, J., Bonavita, M., Chiara, G., Dahlgren, P., Dee, D., Diamantakis, M., Dragani, R., Flemming, J., Forbes, R., Fuentes, M., Geer, A., Haimberger, L., Healy, S., Hogan, R.J., Hólm, E., Janisková, M., Keeley, S., Laloyaux, P., Lopez, P., Lupu, C., Radnoti, G., Rosnay, P., Rozum, I., Vamborg, F., Villaume, S. and Thépaut, J.N. (2020) The ERA5 global reanalysis. *Quarterly Journal of the Royal Meteorological Society*, 146(730), 1999–2049. https://doi.org/10.1002/qj.3803.

Janjić, T., Bormann, N., Bocquet, M., Carton, J.A., Cohn, S.E., Dance, S.L., Losa, S.N., Nichols, N.K., Potthast, R., Waller, J.A. and Weston, P. (2018) On the representation error in data assimilation. *Quarterly Journal of the Royal Meteorological Society*, 144(713), 1257–1278. https://doi.org/10.1002/qj.3130.

Japan Aerospace eXploration Agency. (2015) *AMSR2 Level 1A Product Format Specification*. Tokyo: Japan Aerospace eXploration Agency (JAXA) Retrieved from https://gportal.jaxa.jp/gpr/information/tool.

Jiménez, C., Prigent, C., Ermida, S.L. and Moncet, J.L. (2017) Inversion of AMSR-E observations for land surface temperature estimation: 1. Methodology and evaluation with station temperature. *Journal of Geophysical Research: Atmospheres*, 122(6), 3330–3347. https://doi.org/10.1002/2016JD026144.

Jung, T., Gordon, N.D., Bauer, P., Bromwich, D.H., Chevallier, M., Day, J.J., Dawson, J., Doblas-Reyes, F., Fairall, C., Goessling, H.F., Holland, M., Inoue, J., Iversen, T., Klebe, S., Lemke, P., Losch, M., Makshtas, A., Mills, B., Nurmi, P., Perovich, D., Reid, P., Renfrew, I.A., Smith, G., Svensson, G., Tolstykh, M. and Yang, Q. (2016) Advancing polar prediction capabilities on daily to seasonal time scales. *Bulletin of the American Meteorological Society*, 97(9), 1631–1647. https://doi.org/10.1175/BAMS-D-14-00246.1.

Jung, T., Kasper, M.A., Semmler, T. and Serrar, S. (2014) Arctic influence on subseasonal midlatitude prediction. *Geophysical Research Letters*, 41(10), 3676–3680. https://doi.org/10.1002/2014GL059961.

Jung, T. and Matsueda, M. (2016) Verification of global numerical weather forecasting systems in polar regions using TIGGE data. *Quarterly Journal of the Royal Meteorological Society*, 142(695), 574–582. https://doi.org/10.1002/qj.2437.

Kang, E.J., Sohn, B.J., Tonboe, R.T., Dybkjær, G., Holmlund, K., Kim, J.M. and Liu, C. (2021) Implementation of a 1-D thermodynamic model for simulating the winter-time evolvement of physical properties of snow and ice over the Arctic Ocean. *Journal of Advances in Modeling Earth Systems*, 13(3), e2020MS002448. https://doi.org/10.1029/2020MS002448.

Laroche, S. and Poan, E.D. (2022) Impact of the Arctic observing systems on the ECCC global weather forecasts. *Quarterly Journal of the Royal Meteorological Society.*, 148, 252–271. https://doi.org/10.1002/qj.4203.

Lavergne, T., Eastwood, S., Teffah, Z., Schyberg, H. and Breivik, L.A. (2010) Sea ice motion from low-resolution satellite sensors: an alternative method and its validation in the Arctic. *Journal of Geophysical Research: Oceans*, 115(C10), C10032. https://doi.org/10.1029/2009JC005958.

Lawrence, H., Bormann, N., Sandu, I., Day, J., Farnan, J. and Bauer, P. (2019) Use and impact of Arctic observations in the ECMWF numerical weather prediction system. *Quarterly Journal of the Royal Meteorological Society*, 145(725), 3432–3454. https://doi.org/10.1002/qj.3628.

Lee, S.M. and Sohn, B.J. (2015) Retrieving the refractive index, emissivity, and surface temperature of polar sea ice from 6.9 GHz microwave measurements: a theoretical development. *Journal of Geophysical Research: Atmospheres*, 120(6), 2293–2305. https://doi.org/10.1002/2014JD022481.

Maeda, T., Taniguchi, Y. and Imaoka, K. (2015) GCOM-W1 AMSR2 level 1R product: dataset of brightness temperature modified using the antenna pattern matching technique. *IEEE Transactions on Geoscience and Remote Sensing*, 54(2), 770–782. https://doi.org/10.1109/TGRS.2015.2465170.

Maturilli, M., Holdridge, D.J., Dahlke, S., Graeser, J. and Sommerfeld, A. (2021) Radiosonde measurements in 2020-01 during MOSAiC leg PS122/2 (level 2 data). *Alfred Wegener Institute-Research Unit Potsdam, PANGAEA*. https://doi.org/10.1594/PANGAEA.928659.

Mätzler, C. (1996) Microwave permittivity of dry snow. *IEEE Transactions on Geoscience and Remote Sensing*, 34(2), 573–581. https://doi.org/10.1109/36.485133.

Mätzler, C. (1997) Autocorrelation functions of granular media with free arrangement of spheres, spherical shells or ellipsoids. *Journal of Applied Physics*, 81(3), 1509–1517. https://doi.org/10.1063/1.363916.

Mätzler, C. (1998) Improved Born approximation for scattering of radiation in a granular medium. *Journal of Applied Physics*, 83(11), 6111–6117. https://doi.org/10.1063/1.367496.

Mätzler, C. (2002) Relation between grain-size and correlation length of snow. *Journal of Glaciology*, 48(162), 461–466. https://doi.org/10.3189/172756502781831287.

Mätzler, C. (2005) On the determination of surface emissivity from satellite observations. *IEEE Geoscience and Remote Sensing Letters*, 2(2), 160–163. https://doi.org/10.1109/LGRS.2004.842448.

Mätzler, C. (2006) *Thermal Microwave Radiation: Applications for Remote Sensing*, Vol. 52. Stevenage and Hertfordshire: Institution of Engineering and Technology.

Miernecki, M., Kaleschke, L., Maaß, N., Hendricks, S. and Søbjærg, S.S. (2020) Effects of decimetre-scale surface roughness on L-band brightness temperature of sea ice. *The Cryosphere*, 14(2), 461–476. https://doi.org/10.5194/tc-14-461-2020.

Polder, D. and Van Santeen, J.H. (1946) The effective permeability of mixtures of solids. *Physica*, 12(5), 257–271. https://doi.org/10.1016/S0031-8914(46)80066-1.

Sandu, I., Massonnet, F., Van Achter, G., Acosta Navarro, J.C., Arduini, G., Bauer, P., et al. (2021) The potential of numerical prediction systems to support the design of Arctic observing systems: insights from the APPLICATE and YOPP projects. *Quarterly Journal of the Royal Meteorological Society.*, 147(741), 3863–3877. https://doi.org/10.1002/qj.4182.

Saunders, R., Matricardi, M. and Brunel, P. (1999) An improved fast radiative transfer model for assimilation of satellite radiance observations. *Quarterly Journal of the Royal Meteorological Society*, 125(556), 1407–1425. https://doi.org/10.1002/qj.1999.49712555615.

Semmler, T., Jung, T., Kasper, M.A. and Serrar, S. (2018) Using NWP to assess the influence of the Arctic atmosphere on midlatitude weather and climate. *Advances in Atmospheric Sciences*, 35(1), 5–13. https://doi.org/10.1007/s00376-017-6290-4.

Shokr, M.E. (1998) Field observations and model calculations of dielectric properties of Arctic sea ice in the microwave C-band. *IEEE Transactions on Geoscience and Remote Sensing*, 36, 463–478. https://doi.org/10.1109/36.662730

Tonboe, R.T. (2010) The simulated sea ice thermal microwave emission at window and sounding frequencies. *Tellus A: Dynamic Meteorology and Oceanography*, 62(3), 333–344. https://doi.org/10.1111/j.1600-0870.2009.00434.x.

Tonboe, R.T., Dybkjær, G. and HØYer, J.L. (2011) Simulations of the snow covered sea ice surface temperature and microwave effective temperature. *Tellus A: Dynamic Meteorology and Oceanography*, 63(5), 1028–1037. https://doi.org/10.1111/j.1600-0870.2011.00530.x.

Wang, D., Prigent, C., Kilic, L., Fox, S., Harlow, C., Jimenez, C., Aires, F., Grassotti, C. and Karbou, F. (2017) Surface emissivity at microwaves to millimeter waves over polar regions: parameterization and evaluation with aircraft experiments. *Journal of Atmospheric and Oceanic Technology*, 34(5), 1039–1059. https://doi.org/10.1175/JTECH-D-16-0188.1.

Weng, F., Zou, X., Sun, N., Yang, H., Tian, M., Blackwell, W.J., Wang, X., Lin, L. and Anderson, K. (2013) Calibration of Suomi national polar-orbiting partnership advanced technology microwave sounder. *Journal of Geophysical Research: Atmospheres*, 118(19), 11187–11200. https://doi.org/10.1002/jgrd.50840.

Weng, F., Zou, X., Wang, X., Yang, S. and Goldberg, M.D. (2012) Introduction to Suomi national polar-orbiting partnership advanced technology microwave sounder for numerical weather prediction and tropical cyclone applications. *Journal of Geophysical Research: Atmospheres*, 117(D19), D19112. https://doi.org/10.1029/2012JD018144.

Wiesmann, A. and Mätzler, C. (1999) Microwave emission model of layered snowpacks. *Remote Sensing of Environment*, 70(3), 307–316. https://doi.org/10.1016/S0034-4257(99)00046-2.

World Meteorological Organization's Polar Prediction Project Steering Group. (2013) *WWRP polar prediction project: science plan*. Geneva: World Meteorological Organization (WMO) Retrieved from https://library.wmo.int/index.php?lvl=notice_display&id=15190#.YWAJWtpBxbU.

SUPPORTING INFORMATION

Additional supporting information can be found online in the Supporting Information section at the end of this article.

How to cite this article: Kang, E.-J., Sohn, B.-J., Tonboe, R.T., Noh, Y.-C., Kwon, I.-H., Kim, S.-W. *et al.* (2023) Explicitly determined sea ice emissivity and emission temperature over the Arctic for surface-sensitive microwave channels. *Quarterly Journal of the Royal Meteorological Society*, 149(754), 2011–2030. Available from: https://doi.org/10.1002/qj.4492

APPENDIX

A.1 Relative permittivity

The SSIEM treats the first-year (FY) sea ice and multiyear (MY) sea ice as the pure ice medium embedded with randomly distributed spherical brine pockets and randomly distributed spherical air pockets, respectively, following the recommendations by Shokr (1998). Thus, the relative permittivity can be defined as a mixture of two different permittivities depending on mixing media. For example, in the case of FY sea ice, its relative permittivity (e_{eff}) can be obtained by mixing brine's permittivity (e_2) with that for pure ice (e_1), but scaled with their respective fractions. In SSIEM, the mixing method follows the heterogeneous mixture model by Polder and Van Santeen (1946). Then, the general formula for heterogeneous mixture permittivity can be defined as follows (Mätzler, 1998):

$$e_{\text{eff}} = \frac{e_1 - v(e_1 - e_2) - A(e_1 + e_2) + \sqrt{[v(e_1 - e_2) + A(e_1 + e_2) - e_1]^2 + 4A(1-A)e_1e_2}}{2(1-A)}, \tag{A1}$$

where A is the depolarization factor for the spherical particle and is set to be 1/3. v is the fractional volume of brine which is obtained using temperature (T) and salinity (S_{si}) dependent empirical parametrization (Frankenstein and Garner, 1967):

$$v = S_{\text{si}}\left(\frac{49.185}{T - 273.15} + 0.532\right). \tag{A2}$$

For MY sea ice, a mixture equation similar to Equation A1 can be formulated with permittivities of composing media, but with the fraction v replaced with the

air fraction for MY sea ice. In the SSIEM, the snow is also considered as the air medium embedded with randomly distributed spherical pure-ice pockets. The real part of relative permittivity is parametrized as per Mätzler (1996) and the imaginary part is calculated by the Polder and Van Santeen equation.

A.2 Exponential correlation length

In general, a physical medium is simplified to a geometric dimension with hypothetical simple particle size. Then, understanding how a simple particle relates to the physical medium, this meaningful information is characterized by formulating the exact or approximate expression between electromagnetic waves and medium (Mätzler, 1997). In the SSIEM, as a measure to quantify the strength of the volume scattering of snow and sea ice, exponential correlation length is used as an effective size of particle in terms of the exponential function [i.e. $\exp(-x/p_{ec})$] as autocorrelation function between two components in media with a lag distance of x at the centre of the particle. This leads to an acceptable agreement between the theory and *in situ* data (Debye *et al.*, 1957; Mätzler, 2002).

Under the assumption that snow and sea ice consist of randomly distributed spherical particles with grain size (d in mm), the exponential correlation length (p_{ec} in mm) in the SSIEM is defined as a linear function of d as follows:

$$p_{ec} = F \cdot d, \tag{A3}$$

where F is the conversion coefficient and set to be 0.5.

A.3 Roughness factor

Roughness induces changes in the relative strength of reflectivities for the V/H-pols. The SSIEM handles it as a linear combination based on the linear theory of polarization-dependent wave mixing. For the consideration of the polarization mixing effect, each reflectivity of the V/H-pols (i.e. r_v and r_h) at a specular interface is first calculated using the Fresnel relationships. Then, using the mean reflectivity [i.e. $r = (r_v + r_h)/2$], polarization mixing effect on the reflectivities for both polarizations ($r_{v_{eff}}$ and $r_{h_{eff}}$) are expressed in the linear regime as follows (Wiesmann and Mätzler, 1999):

$$r_{v_{eff}} = r - \Delta r, \tag{A4}$$

$$r_{h_{eff}} = r + \Delta r, \tag{A5}$$

$$\Delta r = \mathfrak{T}\frac{(r_h - r_v)}{2}, \tag{A6}$$

where Δr is a decrement and an increment for V-pol and H-pol. Subscripts v, h and eff represent V-pol, H-pol, and after polarization mixing, respectively. The $\mathfrak{T}$ is a given layer transmittance. This polarization mixing effect is known to be closely related to roughness and some studies define it as a function of roughness (Miernecki *et al.*, 2020).

A.4 Snow and sea ice scattering type

Determining the volume scattering for the snow and sea ice, scattering types were introduced in the SSIEM (based on the MEMLS). In the MEMLS, which is the emission model for the snowpack only, 11 scattering types were introduced and their associated scattering coefficients are determined from physical parameters of snow. Details of the 11 embedded snow scattering types are described in Wiesmann and Mätzler (1999) and references therein. Sea ice scattering and emission were added to the MEMLS, forming a snow/sea ice combined radiative transfer model, SSIEM (Tonboe, 2010). For the sea ice scattering in SSIEM, a single type of sea ice scattering based on "improved Born approximation for spherical inclusion" was introduced (Mätzler, 1998) and its associated scattering coefficient is determined from physical parameters of sea ice.